JOURNAL OF GEOPHYSICAL RESEARCH, VOL. ???, XXXX, DOI:10.1029/,

Rayleigh wave tomography using ambient noise cross-correlations: long period applications in the United States.

G. D. Bensen

Center for Imaging the Earth's Interior, Department of Physics, University of Colorado at Boulder, Boulder, Colorado USA

M. H. Ritzwoller

Center for Imaging the Earth's Interior, Department of Physics, University of Colorado at Boulder, Boulder, Colorado USA

N. M. Shapiro

Laboratoire de Sismologie, CNRS, IPGP, Paris, France

G. D. Bensen, Department of Physics, University of Colorado at Boulder, Campus Box 390, Boulder, CO 80309, USA. (gbensen@colorado.edu)

Abstract. Previous work using ambient noise cross-correlations as computed Rayleigh wave Green's functions showed good results for surface wave tomography at short periods and distances. We extended this work to periods up to 100 seconds period on the scale of the continental United States. Cross-correlations were computed from up to two years of ambient noise recorded at nearly 200 permanent and temporary stations yielding as many as 9,000 acceptable group and phase velocity measurements at a given period. Employing a refined technique that provides uncertainty estimates for each measurement, we show surface wave tomography results at a variety of periods. Resulting group speed dispersion maps at 12 and 40 seconds period as well as phase speed dispersion maps at 25 and 60 seconds period provide information about crustal and mantle structure of the continental United States. Observations of the relative accuracy of group and phase speed tomography results are also presented.

1. Introduction

This study aimed to improve the lateral resolution and short period extent of Rayleigh wave tomography models in the United States using ambient noise cross-correlation tomography. The reliability and popularity of using ambient noise cross-correlations as Green functions has grown quickly in the last several years. Recent theoretical (*Weaver and Lobkis* [2001]) and laboratory (*Derode et al.* [2003]) studies established the technique. The work of *Shapiro and Campillo* [2004] showed initial results for computing reliable Rayleigh wave Green functions between pairs of seismic stations. Such Green functions have been measured to compute tomography maps. The results have proven to be informative in many geographic settings such as Southern California (*Shapiro et al.* [2005]), Europe (*Yang et al.* [2006]), Tibet (*Yao et al.* [2006]), New Zealand (*Lin et al.* [2006b]), Korea (*Kang and Shin* [2006]), and elsewhere. Compared to these previous ambient noise cross-correlation tomography studies, we present results for group and phase speed at longer periods and over a larger geographic area. Data preprocessing to diminish effects of temporal and spectral irregularities helps improve the quality of the cross-correlation waveforms. This improved technique outlined in *Bensen et al.* [2006] allows velocity measurements to longer periods and along longer paths increasing the size of the potential study area. We provide new information about the shear wave structure of the United States and discuss initial observations. Of particular interest are a better understanding of thermal and compositional variations in the dynamic western United States, delineation of sedimentary basins and clearer resolution of crust and mantle features in the eastern United States.

Previous teleseismic surface wave tomography models of the crust and upper mantle were limited by the use of teleseismic earthquake measurements. Several of these studies have been performed in North America (*Alsina et al.* [1996], *Godey et al.* [2003], *van der Lee and Nolet* [1997]). Although these studies used seimograph networks similar to the one used in this study, using only earthquakes as sources was a hindrance for a variety of reasons. The long propagation paths of these events made shorter period (< 20 sec) measurements difficult due to scattering and attenuation; such measurements are necessary for shallower resolution. The fact that most of these earthquakes occurred outside the network made it more difficult to constrain the location of the anomalies in the inversion. The resulting maps from these studies were at 40 seconds period or longer (*Alsina et al.* [1996]) and the shallowest depth reported was 60 km (*van der Lee and Nolet* [1997]). Resulting lateral resolution was on the order of 800 to 1000 km (*Godey et al.* [2003]). Using ambient noise cross-correlation measurements, we provide results to shorter periods (10 seconds period) and with higher lateral resolution (200 km or better).

Another benefit of the cross-correlation technique over teleseismic tomography techniques is the improved path density and azimuthal coverage; this provides higher resolution at all periods. The best resolution would come from a regular grid of stations, including ocean bottom seismometers. The currently developing USArray is such a grid and has been used in a similar analysis (*Moschetti et al.* [2006]) but will not be available for the entire United States until 2014. Other attributes of the ambient noise cross-correlation method increase the measurement precision. Among these are the precise source and receiver locations and known initial phase (*Lin et al.* [2006a]).

Ambient noise tomography is a significant innovation in seismology and provides new information about the Earth with resolution increased by as much as a factor of 10. Using nearly 200 permanent and temporary stations throughout North America, we present results from 10 seconds to 70 seconds period. Our longer period, continental-scale results continue to expand the ambient noise technique and provide new information about the crust and mantle structure of the United States. Based on the findings reported here, we see that the technique is not limited to short periods or regional scales. We resolve shallow features such as sedimentary basins that had not been seen in previous continental scale tomography. Longer period dispersion maps define crustal structure and provide information well into the mantle at depths of 100 km or so. These dispersion maps overlap with previous teleseismic work and should allow continuous imaging from the near surface to hundreds of km depth.

2. Methods and data: from ambient noise to tomography

We followed the technique of *Bensen et al.* [2006] for data processing from raw seismic data (ambient seismic noise) to group and phase dispersion measurements. These measurements were input for a 2D inversion for dispersion maps (*Barmin et al.* [2001]). Using nearly 200 stations from the IRIS DMC and Canadian National Seismic Network (CNSN), we processed any available vertical component broad band seismic data for the selected stations for the 24 month period of March 2003 through February 2005. Stations used appear as black triangles in figure 1a.

Some data preparation was necessary before cross-correlation. Starting with instrument response corrected day-long timeseries at the requested stations; we first performed time-domain normalization to mitigate the effects of large amplitude events. *Bensen et al.*

[2006] divided the raw signal by a smoothed absolute value of itself which retains more of the small amplitude character of the signal than the previous 1-bit technique. A similar whitening normalization was performed on the amplitude spectrum of each day to avoid large inconsistencies in the spectrum. This somewhat improves the visual appearance of the signal but more importantly creates a spectrally smooth signal that enhances the quality of automated broad-band dispersion measurements (see *Bensen et al.* [2006] for more details). After temporal and spectral normalization, cross-correlation was performed on the day-long timeseries yielding two-sided (causal and acausal) Green's functions. The part of the signal containing the Green function is retained and these day results were added for the desired length of input (e.g. one month, one year, etc.). Both the causal and acausal signals are valid Green functions and can be used as input into the measurement routine. For simplicity however, we averaged the causal and acausal signals into a "symmetric signal" to improve the overall signal quality.

These computed Green functions were input into the velocity measurement routine to obtain group and phase dispersion curves. Following *Levshin et al.* [1972], we performed Frequency Time Analysis (FTAN) to measure the phase and group velocity dispersion on all recovered signals. The automated FTAN technique applies a comb of Gaussian filters on a set of periods and measures the group arrival times of these filtered signals. Phase velocity was also measured and further details can be found in *Bensen et al.* [2006]. One note is that a velocity model was needed as input in order to pick the correct branch of the phase velocity to use; even here, a 1D isotropic model would have sufficed. Selected examples of the computed waveforms and resulting group and phase velocity measurements are shown in figures 1b and 1c respectively. The broad-band dispersive nature of

these waveforms is seen in figure 1b with longer period energy arriving first, followed by shorter period energy. Figure 1c shows the resulting group and phase dispersion curves. All curves have the general form of a steep portion which soon levels out to a slowly increasing value. This flatter portion is reached first for phase velocities due to sensitivity to greater depth; the greater depth sensitivity samples faster mantle velocities first at a given period. We see greater deviation from a typical 1D curve at short periods since such waves are less susceptible to the spatial smoothing during propagation.

With measurements through all desired periods for all paths, data selection was begun. The first requirement we imposed was a 3 wavelength minimum interstation distance based on observations of measurement instability at short distances and to fulfill the far field approximation. Next we measured the scatter of measurements on subsets of data. We stacked cross correlations for overlapping 6-month raw timeseries (e.g. June, July, August 2003 plus June, July, August 2004) to obtain 12 "seasonal" stacks and measure the velocity on each of these 6-month stacks in addition to the 24 month stack. As a quality indicator, we defined spectral signal to noise ratio (SPSNR) as the peak signal divided by the RMS noise of a signal filtered to a specified period. Using at least 4, 6-month stacks with a SPSNR higher than 7, we computed standard deviation of the measurements at all periods. Rejection of measurements with a standard deviation greater than 100 meters/second followed. Furthermore, the inverse standard deviation can be used as a weighting factor for the tomographic inversion (see *Bensen et al.* [2006] for more details). *Bensen et al.* [2006] provided proxy information as well to assign standard deviation values when input timeseries are too short to compute directly. Some stations however, did not have sufficient on-time to compute standard deviation so measurements

with SPSNR> 15 were automatically accepted. A final rejection was based on the residuals obtained through the tomographic inversion. Using the accepted measurements, we created an overly smoothed tomographic dispersion map. Paths with high residuals (25 seconds for group dispersion maps and 15 seconds for phase) were removed and the overly smoothed dispersion map was recreated. This became the background dispersion map for a finer inversion. The root mean squared (rms) residuals (in seconds) from these smooth dispersion maps were used to define a new acceptance threshold; paths with residuals greater than 3 times the rms values were rejected. Path retention statistics for selected periods are shown in table 1.

Finally, the accepted measurements were used in the inversion for dispersion maps at selected periods. The tomographic inversion we use is a 2D ray theoretical method described in detail by *Barmin et al.* [2001]. The technique uses a penalty function to decrease the importance of cells with poor path density or azimuthal coverage. For this experiment, we assumed that propagation is along the great circle between stations. The user must choose values for damping (to constrain the amplitude of permitted excursions) and smoothness (to define the spatial roughness allowed). These final 2D dispersion maps provide information about the structure of the continental United States. Also the dispersion maps are a good transferable intermediate product still unaffected by some subjective decisions required for 3D inversion.

The resolution was determined by ray coverage; most important are ray density and azimuthal coverage. Figure 2a shows the resolution map for our 12 second group speed dispersion map. The corresponding ray coverage is shown in figure 2b. More densely instrumented regions, such as southern California and near the New Madrid shear zone in

the central United States, have improved resolution, but, in general, features on the order of 120 km can be resolved through much of the continent. This is a significant improvement from teleseismic models. Still, the edges of the array have quickly degrading resolution. This is seen in regional ambient noise tomography studies as well. This experiment dealt with already available data, but such observations must be taken into account for future array design. Perhaps a tomography routine based on sensitivity kernels incorporating back scattering would extend the resolvable region.

3. Results and discussion

Considering the strengths of this technique listed above, the resulting dispersion maps have higher resolution than teleseismic models. Group dispersion maps at 12 and 40 seconds period and phase dispersion maps at 25 and 60 seconds period are presented. This range covers depths from about 8 km to over 100 km.

A concern when plotting high resolution continental scale tomography is the long wavelength changes in wave speed. In figure 3a, we clearly see the general trend of faster wave speeds in the east than the west. By separating the dispersion map into two halves, each with its own reference wave speed, we are better able to see smaller anomalies. This format is used for all figures. A resolution contour is plotted as a thick black line and areas with low resolution are colored dark grey in figure 3b and following. The actual resolution values are in the figure captions.

The 12-second group dispersion map (figure 3b) has maximum sensitivity to shallower structures of up to 15 km depth. The sediment model of (*Laske and Masters* [1997]) is shown in figure 4 and is useful for comparison. Features mentioned in the text are labeled with letters in figure 4 that are also used below for reference.

Smaller features such as the Central Valley (A) in California and the neighboring fast anomaly associated with the Sierra Nevada (B) indicate the resolution of the dispersion map. General agreement of large/deep basins and low wave speed is observed. Namely we see clear agreement with the Anadarko (C) basin in Texas/Oklahoma and the Permian Basin (D) in west Texas. Deep sediments in the Gulf of Mexico (E) associated with the Mississippi river are seen clearly. Other basins such as the Wyoming-Utah-Idaho thrust belt (F) up to the Williston basin (G) appear clearly. The Appalachian Basin (H) also appears clearly as a slow anomaly. The isolated Michigan Basin (I) is also slightly slower but being not even 3 kilometers deep, it does not affect the Rayleigh waves as much as other basins. The low wave speeds observed in the Basin and Range (J) are interesting considering the lack of deep sedimentary basins. This anomaly is due to thermal or compositional differences rather than sediment overburden.

Looking at longer periods, figure 5 shows a group speed dispersion map at 40 seconds period (figure 5a) contrasted with a phase speed dispersion map at 25 seconds (figure 5b). The depth sensitivity of these two maps is similar and general agreement is observed. With a maximum sensitivity of about 50 km depth they provide information about crustal thickness. The slow anomaly through the Rocky Mountain Region (K) shows the elevated crustal thickness. In the Northern Pacific Coast (L) we observe a slow anomaly likely due to the subducting Juan de Fuca plate. This is not seen farther south where the Farallon slab has already been subducted and some have proposed a "slab window" or thermally different stalled slab (*van Wijk et al.* [2001]). In either case, it is hard to pinpoint a cause of anomaly with wave speed models alone. The effect of the Anadarko basin (C) persists

although it is not of such great depths. Imposition of crustal and sediment thickness constraints in the inversion for 3D structure would confine this anomaly to the crust.

Transitioning to mantle sensitivity, figure 6a shows a phase speed dispersion map at 60 seconds period. This is most sensitive to depths of 100 km or so and shows features of mantle structure and lithospheric thickness. The cold continental craton appears clearly as a fast anomaly while the thermally different structure in the western United States appears at broad scales. The strong signature of the northern and southern Basin and Range (J) is clear, with extensions down around the south side of the Colorado Plateau (K). For comparison, the model of *Shapiro and Ritzwoller* [2002] is shown in figure 6b to illustrate the difference in resolution between the ambient noise correlation and global teleseismic Rayleigh wave tomography methods.

Along with these dispersion maps came information about the quality of the fit of the data and related interpretations. The first type of information was the variance reduction computed from a homogeneous background model. Figure 7 shows the group and phase variance reduction for dispersion maps from 10 to 70 seconds period. The phase velocity measurements provide a strong variance reduction through the entire period range. From 10 to 20 seconds period, similar variance reduction is achieved for group speed dispersion maps as well. Above 20 seconds period, however, phase speed dispersion maps are better fit to the data indicating higher quality measurements. The group velocity measurements show a dip in the variance reduction during intermediate periods (25-60 seconds period). For both group and phase velocity measurements, the mean path length stays nearly the same (around 1800 km) for all periods. The SPSNR of paths used is shown as black dots on figure 7 and although the decline between 15 and 40 seconds seems to follow the

decrease in misfit, a clear relation between variance reduction and SPSNR is not observed. In general, this lull may be a result of the weak background ambient noise amplitudes in the same periods; a clear relation would require more specific research. A similar quality indicator is the final residual in seconds from a smooth input model. Figure 8 shows these values from 10 to 70 seconds period for group and phase speed dispersion maps. Residuals are minimized around 20 seconds period and increase with period from there. The average anomaly amplitude at a given period is higher for group than for phase speed so comparing these residual curves is difficult. Again, the reliability of phase speed dispersion maps is higher above roughly 20 seconds period. This is fortuitous given that group velocity measurements are sensitive to shallower structures. Short period group velocity measurements combined with all measured periods of phase velocity span a large depth range. For the higher quality results, short period group speed maps show the shallowest structure and overlap with phase speed maps; these then extend to over 100 km in maximum sensitivity.

4. Conclusions

We computed cross-correlations of ambient seismic noise to approximate Green's functions between pairs of stations; tomographic inversions of these signals yielded dispersion maps. Cross-correlations were computed from up to two years of ambient noise recorded from March of 2003 to February of 2005 at ∼200 permanent and temporary stations in North America. Dispersion was measured on 2 year stacks as well as subsets of the data; the result is uncertainty values for each measurement. Low standard deviation measurements were retained. After this and other quality control measures, up to 9,000 acceptable measurements remained. These measurements went into a 2D tomographic inversion to

provide dispersion maps. Group and phase speed dispersion maps are obtained from 10 to 75 seconds period. In general, the dispersion maps agree well with expected results and seem geologically accurate. Agreement was observed in many sedimentary basins of sufficient extent and depth, with known crustal thickness and with overall craton structure. Results from data fit to a smooth model show that phase speed dispersion maps are more reliable at periods greater than 20 seconds. Inversion for 3D structure and constraining crustal anisotropy would be natural extensions of this work.

Acknowledgments. All of the data used in this research were downloaded either from the IRIS Data Management Center, the Canadian National Data Center (CNDC). This research was supported by a contract from the US Department of Energy, DE-FC52-2005NA26607, and two grants from the US National Science Foundation, EAR-0409217, EAR-0450082 and EAR-0408228 (GEON project support for Bensen).

References

Alsina, D., R. L. Woodward, and R. K. Snieder (1996), Shear wave velocity structure in north america from large-scale waveform inversions of surface waves, *Journal of Geophysical Research*, *101*(B7), 15,969–15,986.

Barmin, M., M. Ritzwoller, and A. Levshin (2001), A Fast and Reliable Method for Surface Wave Tomography, *Pure and Applied Geophysics*, *158*(8), 1351–1375.

Bensen, G. D., M. H. Ritzwoller, M. P. Barmin, A. L. Levshin, F. Lin, M. P. Moschetti, N. M. Shapiro, and Y. Yang (2006), Processing seismic ambient noise data to obtain reliable broad-band surface wave dispersion measurements, *Geophysical Journal International*, submitted.

Derode, A., E. Larose, M. Campillo, and M. Fink (2003), How to estimate the greens function of a heterogeneous medium between two passive sensors? application to acoustic waves, *Applied Physics Letters*, *83*(15), 3054–3056.

Godey, S., R. Snieder, A. Villasenor, and H. M. Benz (2003), Surface wave tomography of north america and the caribbean using global and regional broad-band networks: phase velocity maps and limitations of ray theory, *Geophysical Journal International*, *152*(3), 620–632.

Kang, T. S., and J. S. Shin (2006), Surface-wave tomography from ambient seismic noise of accelerograph networks in southern korea, *Geophys. Res. Lett.*, *33*, L17303, doi: 10.1029/2006GL027044.

Laske, G., and G. Masters (1997), A global digital map of sediment thickness, *EOS Trans.AGU*, *78*, 483, iD: 10.

Levshin, A., V. Pisarenko, and G. Pogrebinsky (1972), On a frequency-time analysis of oscillations, *Ann. Geophys*, *28*(2), 211–218.

Lin, F., M. P. Moschetti, and M. H. Ritzwollerr (2006a), Phase-velocity measurement of Rayleigh wave based on ambient noise seismology, *Geophys. Res. Lett.*, in preparation.

Lin, F., M. H. Ritzwoller, J. Townend, M. Savage, and S. Bannister (2006b), Ambient noise rayleigh wave tomography of New Zealand, *Geophys. J. Int.*, submitted.

Moschetti, M. P., M. H. Ritzwoller, and N. M. Shapiro (2006), Ambient noise tomography from the first two years of the usarray transportable array: Group speeds in the western us, *Geophys. Res. Lett.*, submitted.

Shapiro, N., and M. Campillo (2004), Emergence of broadband rayleigh waves from correlations of the ambient seismic noise, *Geophysical Research Letters*, *31*(7).

Shapiro, N. M., and M. H. Ritzwoller (2002), Monte-carlo inversion for a global shear-velocity model of the crust and upper mantle, *Geophysical Journal International*, *151*(1), 88–105.

Shapiro, N. M., M. Campillo, L. Stehly, and M. H. Ritzwoller (2005), High-resolution surface-wave tomography from ambient seismic noise, *Science*, *307*(5715), 1615–1618.

van der Lee, S., and G. Nolet (1997), Upper mantle s velocity structure of north america, *J.Geophys.Res*, *102*(B10), 22–815.

van Wijk, J., R. Govers, and K. Furlong (2001), Three-dimensional thermal modeling of the california upper mantle: a slab window vs. stalled slab, *Earth and Planetary Science Letters*, *186*, 175–186.

Weaver, R. L., and O. I. Lobkis (2001), Ultrasonics without a source: Thermal fluctuation correlations at mhz frequencies, *Physical Review Letters*, *87*(13), 134,301.

Yang, Y., M. H. Ritzwoller, A. L. Levshin, and N. M. Shapiro (2006), Ambient noise rayleigh wave tomography across europe, *Geophysical Journal International*, in press.

Yao, H., R. D. van der Hilst, and M. V. de Hoop (2006), Surface-wave array tomography in se tibet from ambient seismic noise and two-station analysis-i. phase velocity maps, *Geophysical Journal International*, *166*(2), 732–744.

Period	Three wavelength	Standard Dev. computed	Standard Dev. < 100 m/sec	SPSNR > 15	Before first tomography	Paths retained
Group						
10	18237	9785	8765	1234	9999	7497
16	17795	11893	10874	1261	12135	9060
25	17342	12149	9975	961	10936	8035
50	15269	5529	3388	910	4298	2940
70	13639	2566	1413	902	2315	1599
Phase						
10	18237	9813	9506	1223	10729	7842
16	17795	9323	8825	995	9820	9181
25	17342	9357	8144	703	8847	8440
50	15269	4560	4269	429	4698	4549
70	13639	2711	2569	421	2990	2824

Table 1. Table 1 lists the number of paths that pass through the different steps of measurement rejection for group and phase measurements. The period is in the first column. The second column shows the paths remaining after rejecting paths shorter than 3 wavelengths. The third column shows the number of paths where standard deviation could be measured. Paths with with standard deviation less than 100 m/sec are in the fourth column. Paths without standard deviation measurements but with a SPSNR greater than 15 are listed in the fifth column. The number of measurements input into the tomography are in the sixth column. The total number of paths after rejection of high residual paths is in the final column.

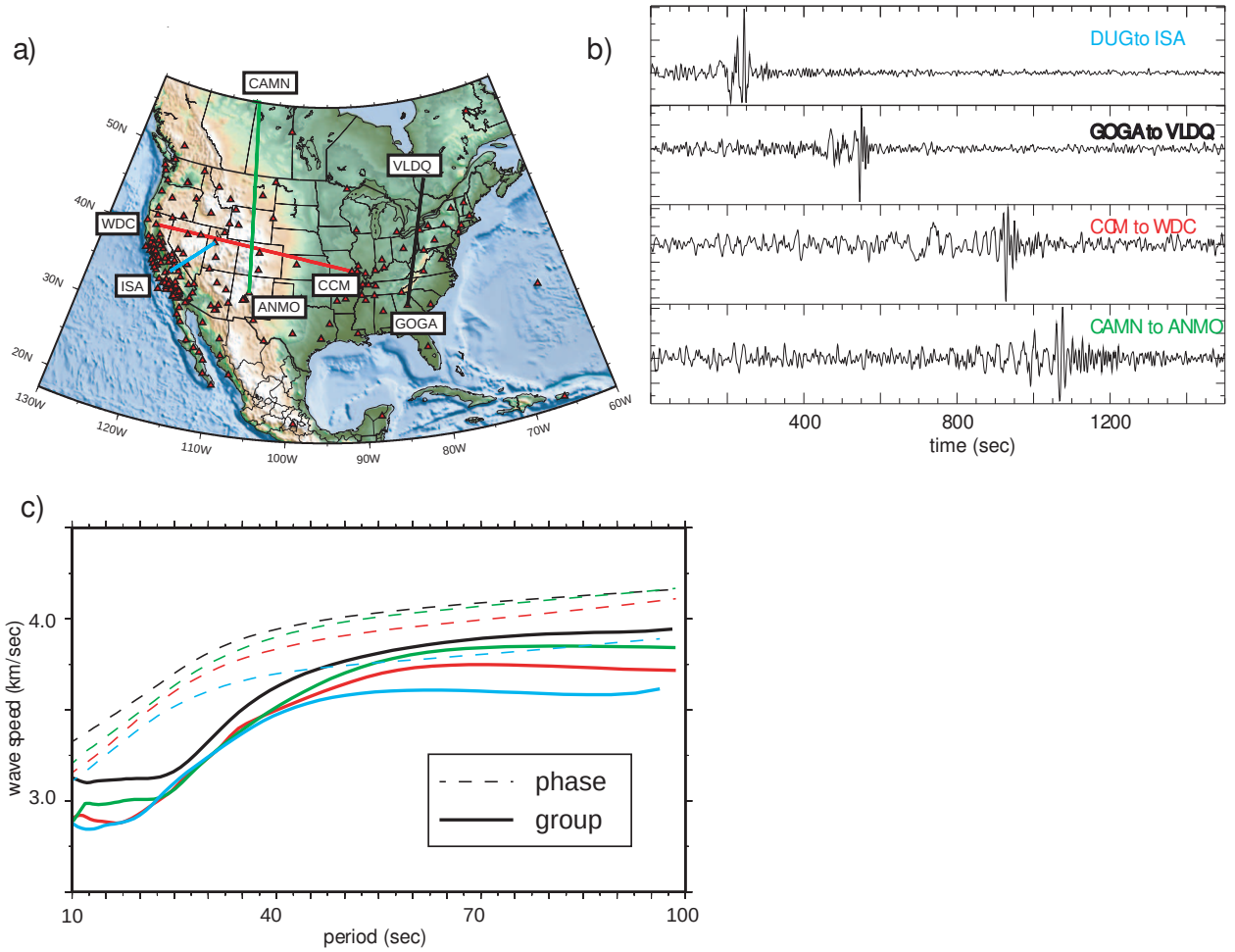

Figure 1. Figure 1a shows the study area with stations used represented as black triangles. The colored paths indicate the paths corresponding the waveforms in 1b and dispersion curves in 1c. Figure 1b shows the broad-band cross-correlations between station RSSD and others. The results are filtered between 7 and 100 seconds period. Figure 1c shows the corresponding group and phase dispersion curves with colors matching those in figure 1a and 1b. Solid lines are group curves and dashed lines are for phase velocity.

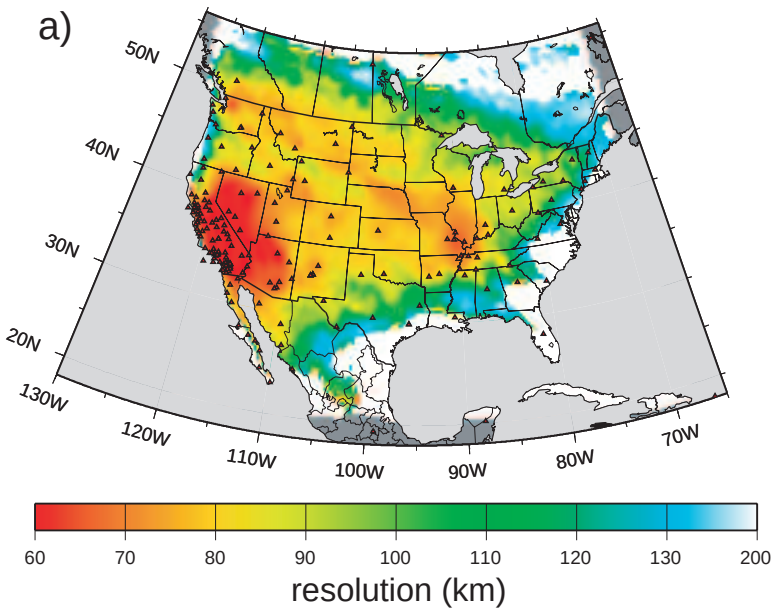

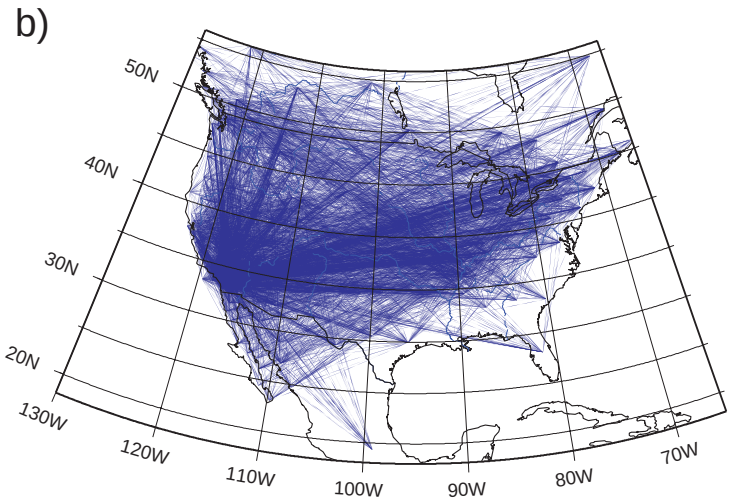

Figure 2. Figure 2a shows the 2 σ resolution map corresponding to the 12 second dispersion map. Stations used in this experiment are shown as triangles. Areas with higher station density such as Southern California and the New Madrid Shear zone have increased resolution while the Eastern Seaboard suffers from low station density. Figure 2b shows that paths used for the 12 second dispersion maps. The resolution map in figure 2a is derived from these paths.

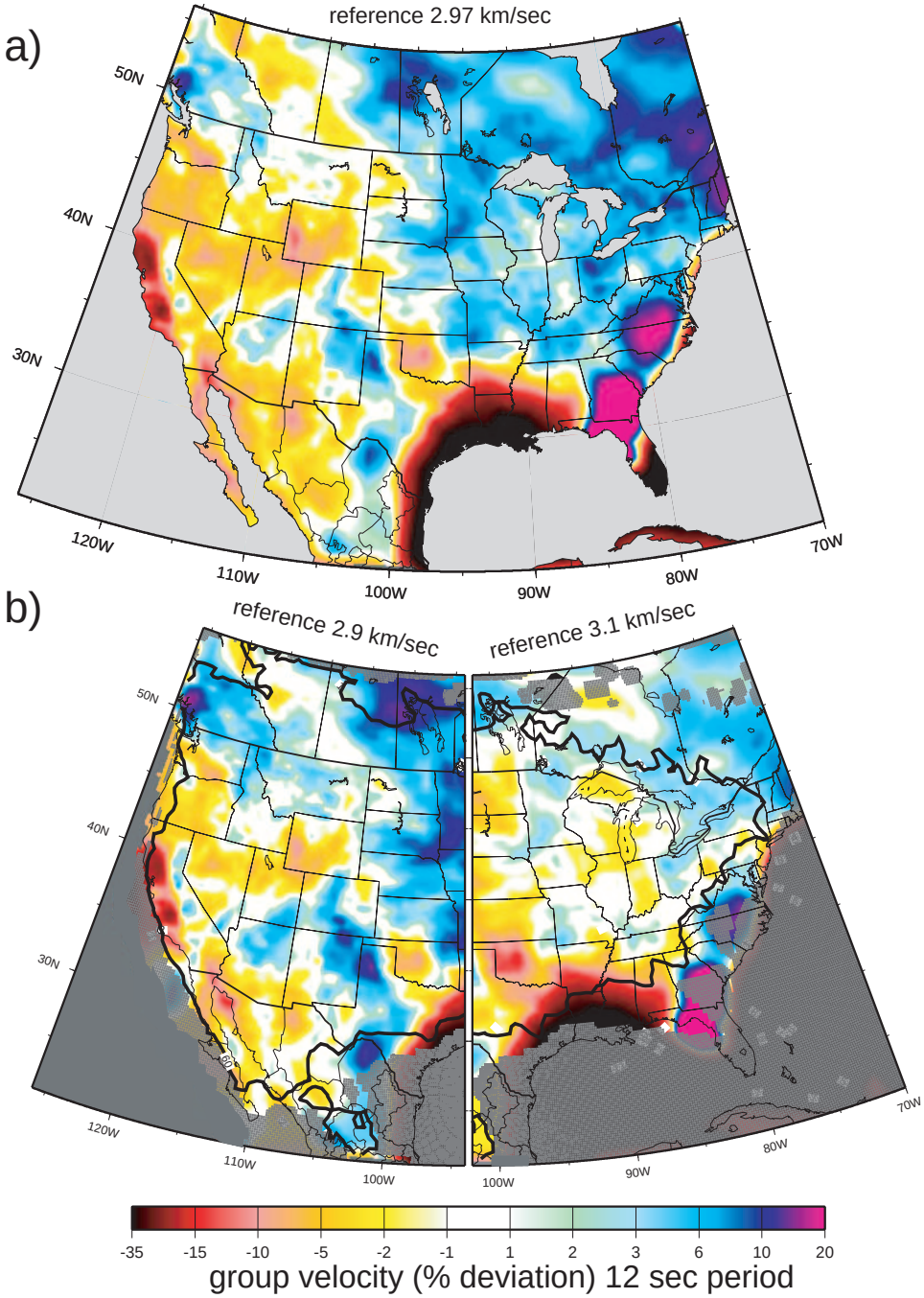

Figure 3. Figure 3a shows a group speed dispersion map at 12 seconds period. Figure 3b shows the same information but with different reference wave speed in the two halves of the image. A higher smoothing parameter was also used in the eastern half since the path coverage is lower. The size of resolvable features is visible. The black contour indicates 120 km resolution and areas with resolution less than 400 km are shaded grey.

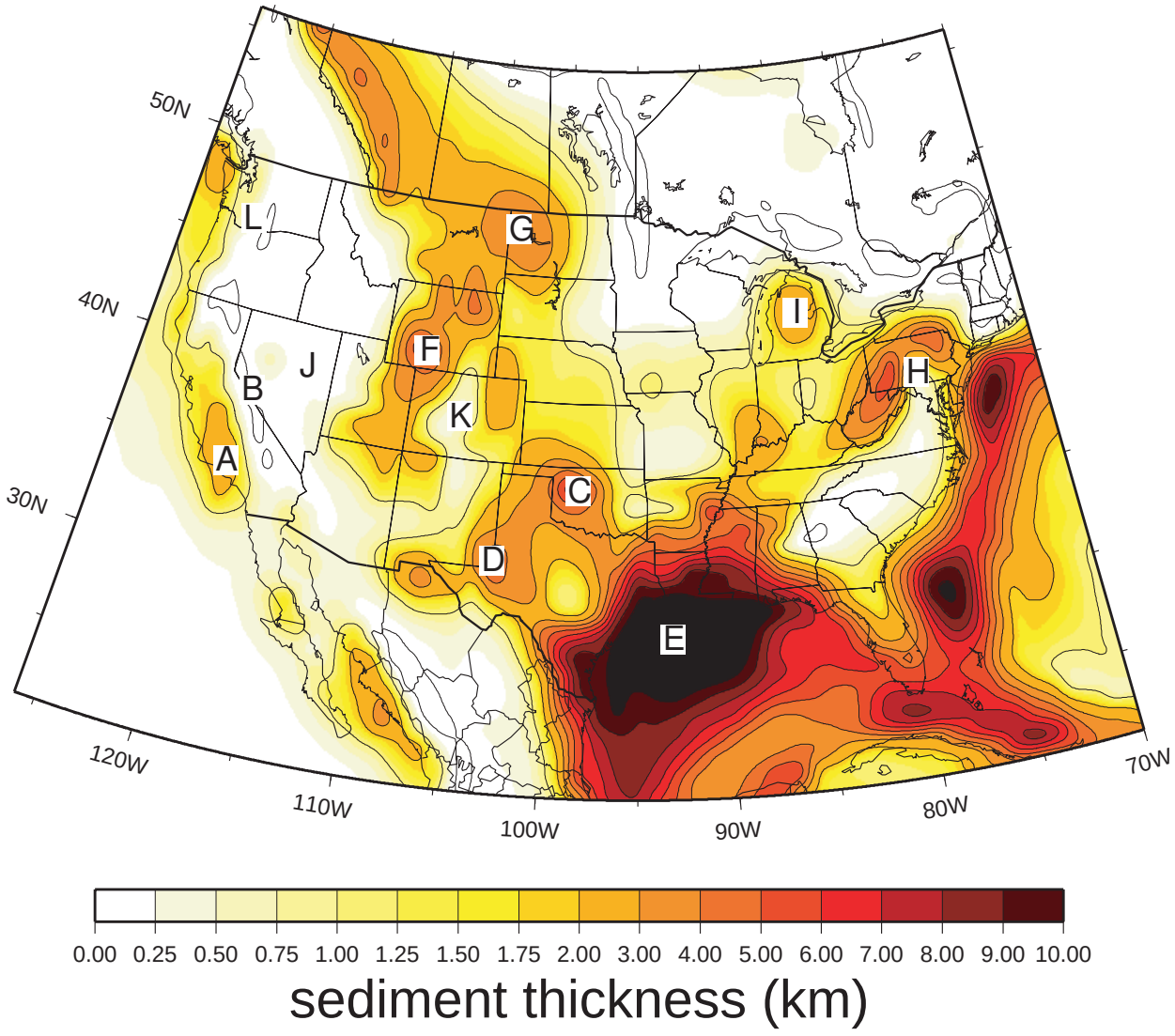

Figure 4. Figure 4 shows the Scripps sediment thickness model *Laske and Masters* [1997] with several prominent features labeled. The features are labeled as follows: 'A' - Central Valley in California, 'B' - Sierra Nevada, 'C' - Anadarko Basin, 'D' - Permian Basin, 'E' - Gulf of Mexico, 'F'- Wyoming-Utah-Idaho thrust belt, 'G' - Williston Basin, 'H' - Appalachian Basin, 'I' - Michigan Basin, 'J' - Basin and Range, 'K' - Rocky Mountain Region 'L' - Northern Pacific Coast.

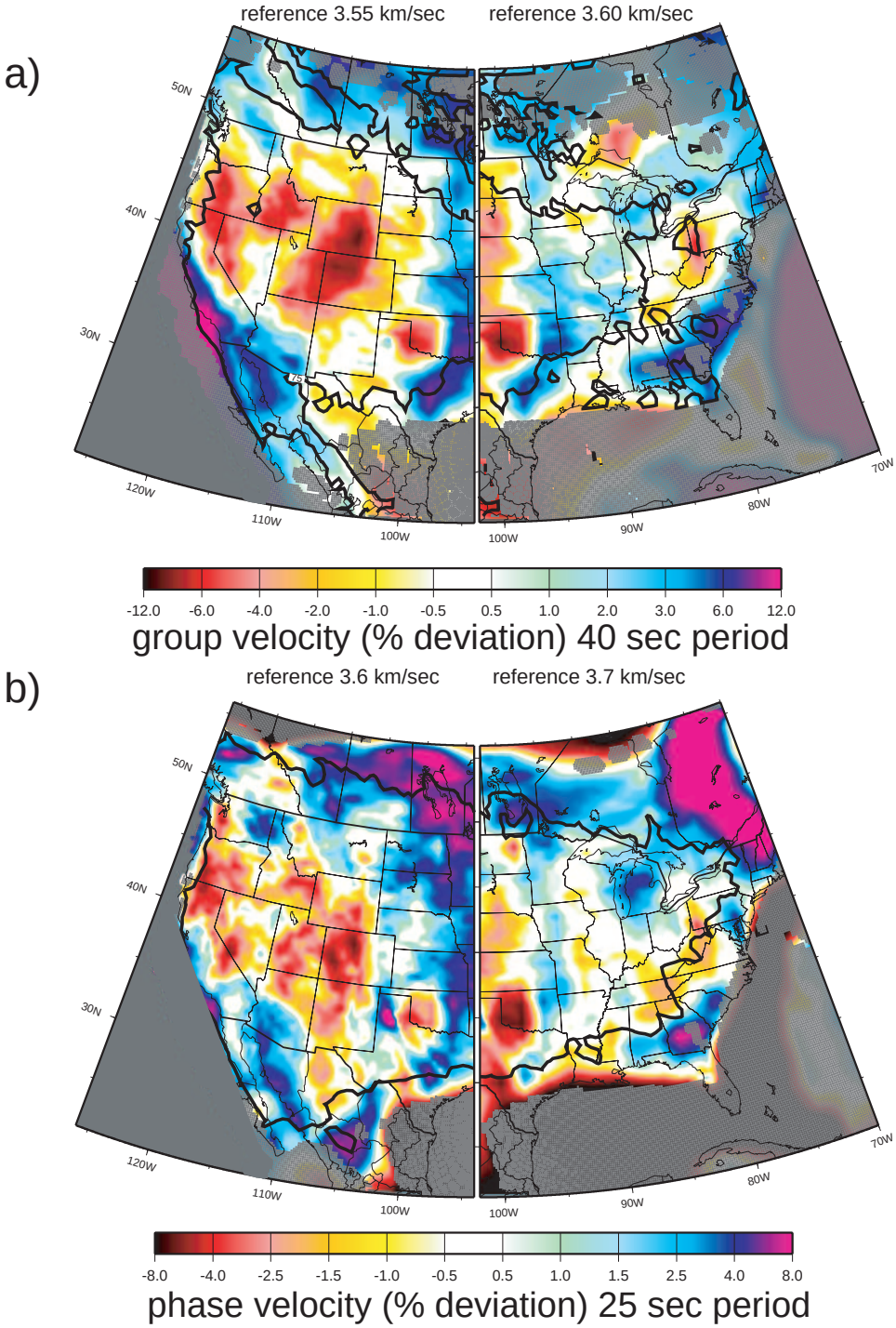

Figure 5. Figure 5a shows the group speed dispersion map at 40 seconds period with the contour indicating resolution greater than 150 km. Resolution less than 500 km is shaded grey. Figure 5b is a phase speed dispersion map at 25 seconds period. The black contour indicates resolution of 120 km and resolution less than 400 km is shaded grey. Different reference wave speeds are used in each half of the map and are indicated in the figure. These two dispersion maps have similar depth sensitivities and general agreement is observed.

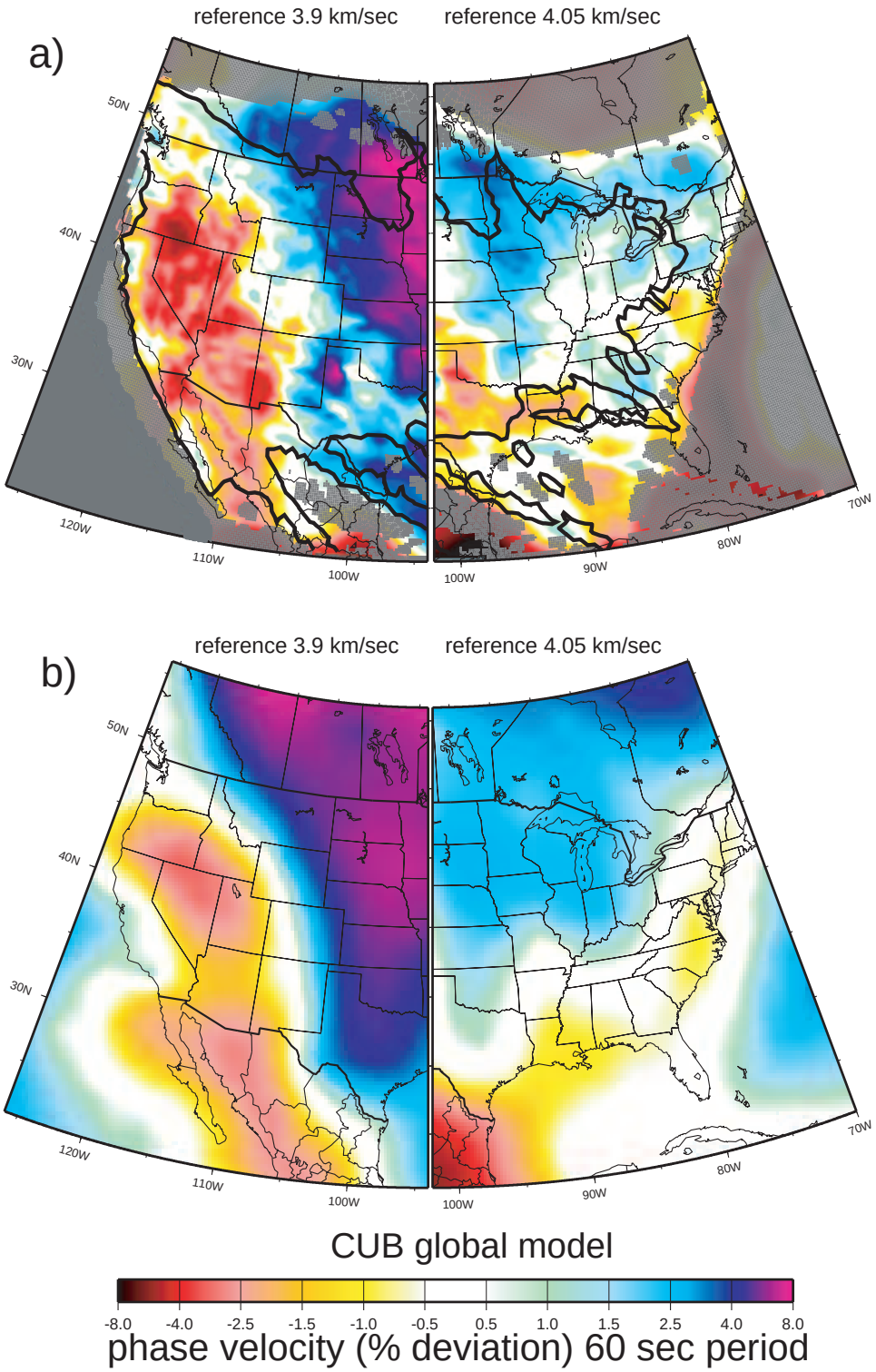

Figure 6. Figure 6 a shows the phase speed dispersion map at 60 seconds period with the black contour showing 150 km resolution and again, regions with resolution less than 500 km are shaded grey. For comparison, the CU global model (*Shapiro and Ritzwoller* [2002]) is shown in figure 6b with the same color scale and reference wave speed.

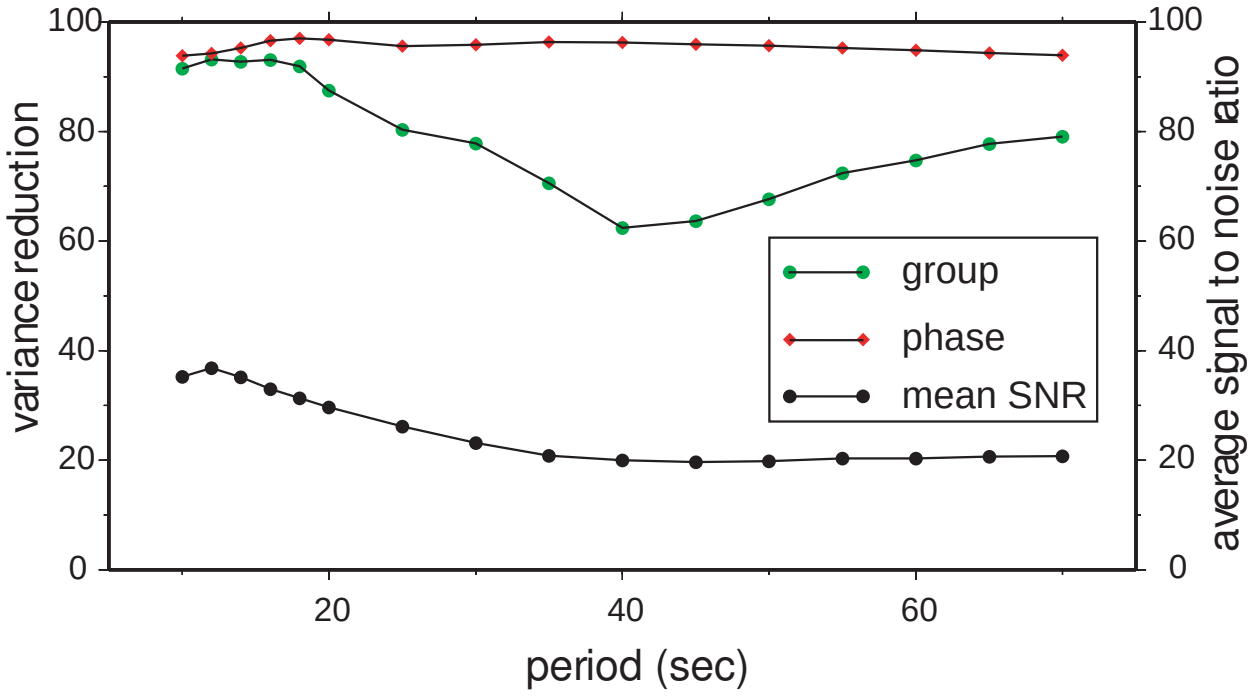

Figure 7. Figure 7 shows the variance reduction for group (green dots) and phase (red diamonds) speed dispersion maps through a range of periods. This is computed from a homogeneous background model. The variance reduction for the phase velocity measurements is high through all periods while it is more variable for group velocity measurements. The mean SNR at each period for both group and phase velocity measurements are similar and are shown with black dots. The group velocity measurements are more sensitive to a reduction in SNR.

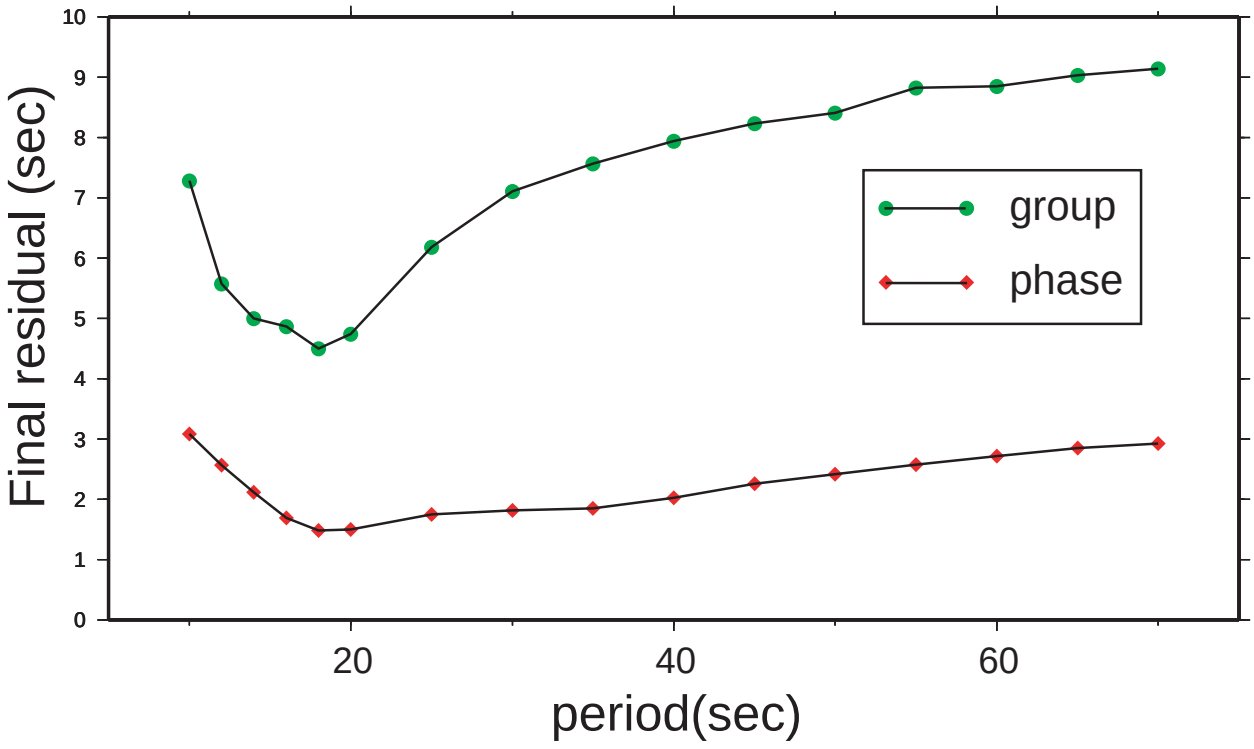

Figure 8. Figure 8 shows the final residuals from a homogeneous background model for group and phase speed dispersion maps. Group values are in green and phase are in red. Above 20 seconds period, the phase speed residuals grow more slowly indicating higher precision measurements.